J. Non-Newtonian Fluid Mech. 166 (2011) 194–207

Contents lists available at ScienceDirect

Journal of Non-Newtonian Fluid Mechanics

journal homepage: www.elsevier.com/locate/jnnfm

Rheology of wormlike micelles from non-equilibrium molecular dynamics

J. Castillo-Tejas[a,*], J.F.J. Alvarado[b], S. Carro[a], F. Pérez-Villaseñor[a], F. Bautista[c], O. Manero[d]

[a] Facultad de Ciencias Básicas, Ingeniería y Tecnología, Universidad Autónoma de Tlaxcala, Calzada Apizaquito S/N, Apizaco, Tlaxcala, 90300, Mexico
[b] Departamento de Ingeniería Química, Instituto Tecnológico de Celaya, Avenida Tecnológico y García Cubas S/N, Celaya, Guanajuato, 38010, Mexico
[c] Departamento de Ingeniería Química CUCEI, Universidad de Guadalajara, Boulevard M. García Barragán No. 1451, Guadalajara, Jalisco, 44430, Mexico
[d] Instituto de Investigaciones en Materiales, Universidad Nacional Autónoma de México, Ciudad Universitaria, Distrito Federal, 04510, Mexico

ARTICLE INFO

Article history:
Received 17 May 2010
Received in revised form
11 November 2010
Accepted 18 November 2010
Available online 24 November 2010

Keywords:
Non-equilibrium molecular dynamics
Wormlike micelles
Banding transitions

ABSTRACT

In this work, the rheology of complex fluids, i.e., surfactants of varying concentration in a Lennard–Jones fluid, is analyzed with non-equilibrium molecular dynamics simulations. The molecular model considers that the surfactant molecule is composed of a hydrophilic head, affine to solvent, and a hydrophobic tail made of four monomers. The solvent is modeled by a Lennard–Jones fluid, which shows mostly a Newtonian behavior, but at relatively high shear rates, a slight shear-thinning followed by a slight shear thickening are exhibited. The intermolecular potential produces an equilibrium configuration, in which the surfactant molecules self-assemble in a wormlike micelle. With the aim to analyze the system behavior with various stress fields, two flows are simulated under non-equilibrium conditions: (1) simple shear and (2) Poiseuille's flow. In simple shear, by keeping the velocity of the upper plate of the flow cell constant, a monotonic flow curve is predicted within a range of shear rates. At low shear rates, a concentration-dependent Newtonian region of viscosity η_0 corresponds to an isotropic condition in which the wormlike micelle preserves its equilibrium conformation. At intermediate shear rates, the solution exhibits a slight shear thinning, generating bands placed normal to the gradient direction (gradient banding). At high shear rates the solution exhibits shear-thickening, with bands now generated normal to the vorticity direction. These predictions by molecular models explain, to our knowledge for the first time, experiments in shear-thickening wormlike micellar solutions, where shear-thickening appears simultaneously with bands generated perpendicular to the vorticity axis. In Poiseuille's flow, we also find agreement between predictions of the model with theoretical developments and experiments performed by other authors.

1. Introduction

Due to their unique viscoelastic properties, wormlike surfactants are used in many industrial applications, like viscosity modifiers, emulsifiers, lubricants and drilling fluids in the oil industry. The surfactant molecules possess polar head groups that have affinity to the solvent (hydrophilic) and non-polar tail groups that are hydrophobic. They self-assemble to form aggregates of relatively large size. The complex rheological behavior of micellar solutions is a consequence of micellar growth, micellar interactions and dynamics of orientation under flow [1]. In addition, its rheological behavior is related to the continuous processes of breakage and reformation of the giant micelles [3–6]. Micelles grow with increasing surfactant concentration according to thermodynamic considerations [2]. It is convenient to distinguish three concentration regimes: dilute, semi-dilute and concentrated. The dilute regime ends at the so-called overlapping concentration c^*, and the semi-dilute concentration spans from c^* to concentrations where the entangled network has mesh sizes larger than the persistence length, typically around 10 wt.% for common surfactant systems. Above c^*, the long and flexible wormlike micelles can form entanglements similar to polymer solutions. Under flow, one of the most interesting rheological phenomenon is that related to the appearance of banding transitions, one along the gradient direction ("gradient banding") and another one directed along the vorticity direction ("vorticity banding"). *Gradient banding* is associated to the shear thinning region in the flow curve, stress versus shear rate, where two spatially different flow bands with different shear rates coexist in the stationary state. In each of the two bands, the velocity gradient is essentially constant, independent of position [7]. Experimentally, shear-banding flow has been studied mostly in solutions of giant micelles with flow visualization techniques, NMR and rheometry. Rehage and Hoffmann [6,8] found a stress plateau which was also observed in various flow geometries [9–16]. Salmon et al. [17], using dynamic light scattering, found that the viscosity drop in the system is due to the nucleation and growth

* Corresponding author. Tel.: +52 241 41 72544; fax: +52 241 41 75844.
E-mail address: j_castillo_tejas@hotmail.com (J. Castillo-Tejas).

0377-0257/$ – see front matter © 2010 Elsevier B.V. All rights reserved.
doi:10.1016/j.jnnfm.2010.11.009

of a highly sheared band. Usually, shear banding is attributed to an underlying shear-induced transition from a given microscopic organization of the fluid structure into another one. Shear induced transitions are often associated to very complex phenomena [18]. For example, in concentrated wormlike solutions like CTAB/D_2O, three-dimensional flow patterns were found [19]. Boundary conditions and temperature affect the velocity profiles, gradient-banding and modify the rheological behavior of the system [20–22]. In pressure-driven Poiseuille's flow, experiments on flow visualization show regions of turbidity [23], lying almost parallel next to the wall, growing toward the channel center with increasing wall shear rate. These layers can be associated with a secondary flow comprising velocity rolls [24]. Finally, the molecular origin of *gradient-banding* is suggested to be associated to orientation, disentanglement of the micellar aggregates and micellar growth [25], particularly in concentrated solutions, but a microscopic account of the fluid configuration in each band is still lacking.

The other *banding transition,* know as "vorticity banding", occurs when the system forms bands normal to the vorticity direction. This phenomenon has been observed when the flow curve tends to a shear-thickening regime. In the cetylpyridinium chloride–sodium salycilate solution (CPyCL and NaSal), Fischer et al. [26] and Herle et al. [27,28] report the formation of bands normal to the vorticity direction. The flow curve below a critical shear stress τ_c exhibits Newtonian behavior followed by shear-thinning. Above τ_c, the solution exhibits shear-thickening with alternating turbid-transparent bands along the vorticity axis. Using small-angle neutron-scattering under flow (Rheo-SANS) and video imaging, Herle et al. found anisotropic patterns in both bands, indicating strong alignment of the structures; notwithstanding, the micellar alignment does not correspond to the lower viscosity band. Vorticity banding has also been observed in colloids [29–31], wherein experiments suggest the association of vorticity banding to an elastic instability similar to the Weissenberg effect [31], implying a relation between the band apparition and normal stresses along the gradient axis. The vorticity structuring has been also associated to velocity rolls stacked along the vorticity direction [32]. In summary, *vorticity banding* is less understood and no theoretical tools are yet available to predict its apparition and its relation to the flow field.

During the recent decade, molecular simulation has emerged as an important theoretical tool in material science and in rheology of complex fluids. Qualitative understanding of polymeric systems has been improved and quantitative account of transport processes in simple molecules such as alkenes has been described. Molecular simulation techniques are becoming widely used for the study of rheological and structural properties in system formed by complex molecules, such as polymers [33–37] and alkanes [38–40]. Non-equilibrium molecular dynamics (NEMD) simulations aim to establish a connection between the molecular structure of the system and its rheological response. In simple shear simulations for linear molecules [41], the static structure factor calculations show agreement with experiments. On the issue of *shear-induced particle structures*, there is a notorious similarity between the SANS dispersion patterns for polymer solutions under simple shear and Poiseuille's flows and NEMD simulations for a soft sphere model fluid [42].

In micellar systems, Kröger and Makhloufi [43] suggested that the FENE-C model can be used to predict the rheological behavior of systems of giant micelles, in which the breakage–reformation process of the micelles is included. Non-equilibrium molecular dynamics simulations predicted the dependence of the micellar length distribution on the flow. Using the same model, Padding and Boek [44] studied the flow-induced formation of micellar rings and wormlike micelles. Predictions show that at low concentrations, ring-like micellar structures predominate, while linear chains dominate at high concentrations. However, the model predicts a shear-thinning viscosity with slope of −0.4, different to the expected slope of −1 in micellar systems. In a latter paper, Padding et al. [45] used Brownian dynamics to predict flow curves of such systems. Recently, coarse-grained molecular models have been used to predict structural properties of solutions of giant micelles [46–48].

It is important to mention that the selected molecular model for giant micelles must be able to describe three basic issues: the interaction among the various micellar aggregates to form a wormlike micelle, alignment of the aggregates along the flow direction with a migration process to form bands, and the entanglement–disentanglement dynamics. In this work, the flow of micellar solutions, in simple shear and Poiseuille's flows, is analyzed using non-equilibrium molecular dynamics simulations. The main objective is the prediction of the *banding transitions*, observed in the experiments, and to establish the relation between molecular organization and rheological behavior. It is important to point out again that the molecular model used here addresses the dynamics of interaction, orientation and migration under flow. For the system size selected, it does not consider the entanglement–disentanglement process in more concentrated solutions. The manuscript is organized as follows: Section 2 presents the molecular model and the equations of motion to simulate the flow. Section 3 includes a description of the system, geometry and simulation conditions and presents calculations of the rheological properties. Section 4 discusses the flow behavior of the solutions under simple shear and Poiseuille's flow and shows results about the banding formation along gradient and vorticity directions. An analysis of the structural changes is provided as functions of the shear rate. Finally, in Section 5, the main conclusions are presented.

2. Theory and simulation method

2.1. Equation of motion

In a system where positions and velocities evolve at constant volume and temperature (using a Nosé–Hoover thermostat), the equations of motion are:

$$\frac{d\mathbf{r}_i}{dt} = \mathbf{v}_i \tag{1}$$

$$\frac{d\mathbf{v}_i}{dt} = \frac{\mathbf{F}_i}{m_i} - \xi\mathbf{v}_i \tag{2}$$

$$\frac{d\xi}{dt} = \frac{1}{Q}\left[\sum_i \frac{{p_i}^2}{2m_i} - LT\right] \tag{3}$$

where $\mathbf{r}_i$, $\mathbf{v}_i$, $\mathbf{F}_i$ are the position, velocity and force on a particle i, T is the objective temperature of the system, L the degree of freedom, Q the thermostat mass and ξ is the thermodynamic friction coefficient. Solution of Eqs. (1)–(3) allows knowing the position and velocity of a particle at any instant and under *equilibrium conditions*. Under non-equilibrium conditions and taking into account the concept of peculiar velocity, the degrees of freedom of the thermostat are given by $L = 2N$, where N is the number of segments in the system. An important parameter related to the efficiency of the thermostat is its mass Q. This is defined as $Q = LT\tau^2$, where T is the temperature and τ is the relaxation time of the system [49].

With the aim to analyze the system behavior with various stress fields, two flows are simulated under *non-equilibrium conditions*: (1) simple shear and (2) Poiseuille's flow. In molecular dynamics, the flow condition is simulated by adding an external term (external perturbation) to the equations of motion or by modifying the system boundaries. In this work, a Poiseuille flow is generated by

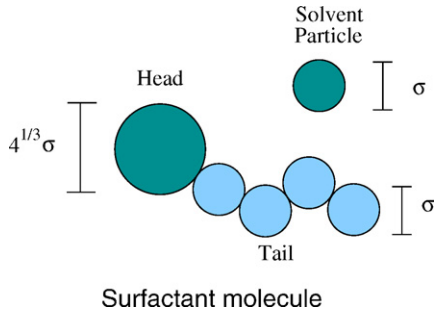

Fig. 1. Schematic representation of the surfactant molecule.

adding the term $\mathbf{i}F_e$ to the right of Eq. (2). The unit vector $\mathbf{i}$ represents the flow direction and F_e is an external force field (equivalent to the pressure gradient). For a simple shear flow, the flow is generated by modifying one of the system boundaries, as detailed in Section 3.2.

Finally, the solution of the system of differential equations is performed with the *reversible explicit system propagator algorithm* (RESPA) [49], where the factorization of the Liouville operator is carried out according to Xu et al. scheme [36]. Likewise, the velocity established by the Liouville operator for the dynamic variables of the thermostat occurs within the same time scale of the reference system.

2.2. Molecular model

Dense macromolecular systems, such as the systems given attention here, are difficult to implement due to the variety of chemical species that form the molecule, which imply numerous and different interactions among those species contributing to the calculation of the system energy. With the aim to reduce the complexity of the molecular model, in this work we use a model of the *Coarse-Grained* type [46]. With this molecular model is possible to generate a wormlike micelle that is stable and independent of the periodic boundary conditions [47]. Surfactant molecules present a double character, a hydrophilic head affine to polar solvents and a hydrophobic chain affine to organic solvents. The model proposed here assigns to the hydrophilic head a diameter of $4^{1/3}\sigma$, while the hydrocarbon hydrophobic chain is composed of four sites each one with diameter σ (see Fig. 1). To reproduce the chemical bond between sites or monomers forming the molecule, a harmonic potential is used:

$$U_{enl}(r_{ij}) = 5000(r_{ij} - \sigma_{ij})^2 \tag{4}$$

where ε is an energy-level parameter, and σ_{ij} is calculated using the Lorentz–Berthelot combining rules given by the following equation $\sigma_{ij} = 0.5(\sigma_{ii} + \sigma_{jj})$. The solvent is modeled according to a Lennard–Jones-type potential corresponding to a soft sphere of diameter σ. The solvent–solvent, solvent–hydrophilic head, and hydrophilic head–head interactions and those between hydrophobic tails is modeled again according to a Lennard–Jones potential given by

$$U_{lj}(r_{ij}) = 4\varepsilon\left[\left(\frac{\sigma_{ij}}{r_{ij}}\right)^{12} - \left(\frac{\sigma_{ij}}{r_{ij}}\right)^{6}\right] - U_{lj}(r_c) \tag{5}$$

Likewise, the hydrophobic tail–solvent interactions and the head–hydrophobic tail interactions are simulated according to a repulsive potential given by

$$U_{rep}(r_{ij}) = \varepsilon\left[\frac{1.05\sigma_{ij}}{r_{ij}}\right]^{9} \tag{6}$$

The parameter $1.05\sigma_{ij}$ is fixed taking into account that the hard-core repulsion is approximately as strong as repulsive part of Lennard–Jones potential (for more details see Ref. [46]). The non-bonding interactions given by the Lennard–Jones potential are truncated and smoothed at a cut-off radius of $r_c = 2.5\sigma_{ij}$.

3. Simulations details and methodologies

3.1. Reduced properties

The system variables are expressed in terms of reduced quantities with respect to the mass (m_i), energy (ε) and length (σ), to which a value of one is assigned ($\varepsilon = \sigma = m_i = 1.0$). This formulation has the advantage that the principle of corresponding states can be applied [50]. The mass is expressed in units of atomic mass, the energy is given in units of the depth of the well potential and the lengths are referred to the particle diameter. The reduced expressions for the relevant parameters are [51]: $\rho^* = \rho\sigma^3$, $T^* = k_B T/\varepsilon$, $U^* = U/\varepsilon$, $\mathbf{P}^* = \mathbf{P}\sigma^3/\varepsilon$, $t^* = t(\varepsilon/m\sigma^2)^{1/2}$, $\dot{\gamma}^* = (m\sigma^2/\varepsilon)^{1/2}\dot{\gamma}$ and $\eta^* = (\sigma^4/m\varepsilon)^{1/2}\eta$, where ρ is the local density, k_B is the Boltzmann constant, U is the energy, $\mathbf{P}$ is the pressure tensor and t is time. For simplicity, hereafter the asterisk notation will be omitted.

3.2. System and geometry

The systems analyzed in this work consist of M surfactant molecules, each one containing five sites, and S solvent particles affine to the hydrophilic head groups. According to the molecular model, each molecule in turn contains N_c sites connected by harmonic springs. The total number of sites in the system is $N = MN_c + S$. For the simulations, the system size N comprises 6000 sites (molecules and solvent sites) with a reduced density per site of 0.66 and reduced temperature of 1.35. The reduced density ρ is the ratio of the total number of sites and simulation volume, and together with the number of sites in the system, the simulation domain in defined.

In this work we use a *Coarse-Grained*-type molecular model, by which it is possible to assemble various *spherical micelles* under equilibrium, and furthermore, a *wormlike micellar structure* may also be formed under flow. This choice considers the experimental measurements of the characteristic length of a spherical micelle, which varies in the range of 2.5–20 nm [52], and that of the persistence length of a wormlike micelle, which varies from 15 to 150 nm [53,54]. In molecular dynamics, the size of the computational domain must be sufficiently larger than the characteristic molecular lengths of the system under study. On the basis of the molecular model and the concept of reduced units, the reference molecular segment may include up to three or more CH_2 groups. As a first approximation, the reference segment would have a size of 0.9 nm, such as one side of the simulation domain would be around 19 nm. This length scale is appropriate to the characteristic length of the spherical and wormlike micelles.

Five study cases have been selected, with site concentrations of 0.0, 0.05, 0.10, 0.15 and 0.20. The concentration per site ϕ is the ratio of the solute number of the sites and the total number of the sites (solute and solvent) used in molecular simulations works on micellar solutions [43,44]. To define the concentration regime, the overlap concentration c^* is that corresponding to twice the solvent viscosity. On the basis of the flow curves shown in Section 4.1.1, only the solutions with concentrations of 0.05 and 0.10 are found in dilute regime.

The geometry of the simulation region is shown in Fig. 2, with dimensions given in terms of σ units. Walls are found parallel to the x–y plane normal to the gradient axis. The two flows are generated along the x axis, with the velocity gradient placed along the

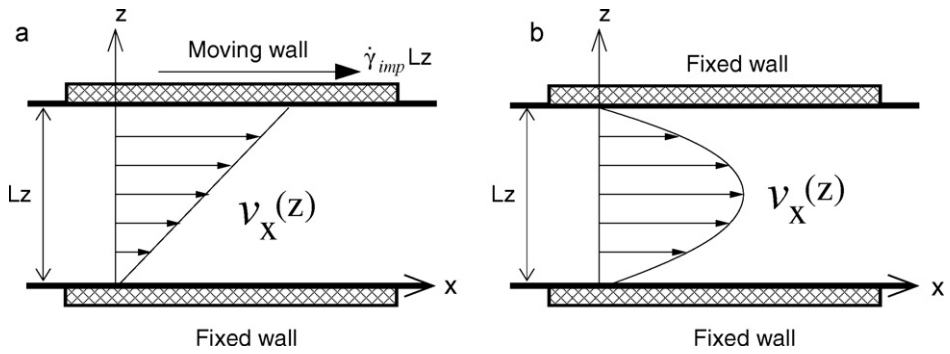

Fig. 2. Schematic representation of the simulation region between parallel surfaces: (a) simple shear flow and (b) Poiseuille's flow.

z direction and the vorticity axis placed along the y direction. The periodic boundary and minimal image conditions are applied only along the flow and vorticity directions.

To simulate the effect of the fixed surface (lower wall in simple shear and both walls in Poiseuille's flow), a particle crossing any of the walls located in the x–y plane is reflected to the flow domain. The surface roughness is simulated assigning the particle with a random velocity scaled at the system temperature [55]. However, the moving boundary in simple shear is simulated by considering that any particle exiting the upper wall is reflected to the flow domain with a velocity $\dot{\gamma}_{imp}L_z$, where $\dot{\gamma}_{imp}$ is the imposed shear rate and L_z is the length of the simulation region with value of 20.89σ. Again in simple shear, the origin is located at the center of the lower wall, $z=0$, and the upper wall is located at $z=L_z$. For Poiseuille's flow, the origin is found at the middle of the simulation region, such that the walls are located at $z=\pm 0.5L_z$.

In practice, Poiseuille's flow is generated by a pressure gradient. However, in molecular simulations the pressure gradient is substituted by an external force F_e. For the *Poiseuille's flow* simulations, the magnitude of the external force F_e varies from 0.1 to 0.3. In molecular simulations, the magnitude of F_e to generate the flow depends on the fluid type, confinement distance, density and geometry. However, it is important to mention that the peak velocities obtained in previous works [56,57] is similar and independent of the magnitude of the external force within this range. For the *simple shear flow* simulations, the magnitude of the imposed shear rate $\dot{\gamma}_{imp}$ varies from 0.001 to 13.0.

Finally, the initial configuration of the non-equilibrium molecular dynamics simulation is equilibrated for the quiescent state in rectangular simulation regions. The number of integration steps amounts to 10 million with a time step $\Delta t=0.001$. In Fig. 3, the *equilibrium configuration* corresponding to a system with $\phi=0.15$ is depicted. Green dashed dots, blue dots and red dots represent the solvent, hydrophilic heads and hydrophobic tails, respectively. Such configurations show the spherical micelles assembled, with its hydrophobic tails (red dots) pointing inwards repelling the solvent (green dots). It is important to mention that the wormlike configuration is stable and its survival does not depend on the periodic boundary conditions. This configuration is the initial step for the non-equilibrium simulations. The non-equilibrium simulations take 10 million integration steps, of which the first 5 million are necessary to equilibrate the system under shear flow. For the range of shear rates imposed $\dot{\gamma}_{imp}$ and external force F_e considered, the time step is fixed to $\Delta t=0.001$.

3.3. Stress tensor

The relationship between molecular structure and stress field is a necessary condition to describe the rheological behavior of the system. In this work, the plane method for non-homogeneous flow [56] is used to calculate the pressure tensor in the fluid, according to the following expression:

$$P_{zx}(z)=\frac{1}{A}\left\langle\sum_{i=1}^{N}\frac{p_{zi}p_{zi}}{m_i}\delta(z-z_i)\right\rangle+\frac{1}{2A}\left\langle\sum_{i=1}^{N}F_{xi}sgn(z_i-z)\right\rangle \quad (7)$$

where P_{zx} is the pressure tensor component acting along direction x through a plane normal to the z axis. A is the area of the plane normal to the z axis, $\mathrm{sgn}(z_i-z)$ is equal to one if $(z_i-z)>0$ and to -1 if $(z_i-z)<0$. Moreover, F_{xi} is the x-component of the force acting on particle i, and p_{zi} is the z component of the momentum of particle i, respectively. The stress tensor $\mathbf{T}$ is related to the non-equilibrium components of the pressure tensor such that $\mathbf{T}=-\mathbf{P}$. The total stress $\mathbf{T}$ implies the contribution of the pressure and that of the viscous stress, such that $\mathbf{T}=p\mathbf{I}+\tau$. The plane method allows calculating the stress components τ_{zx} in the computational domain.

4. Results and discussion

Results were obtained for a number of time-averaged fluid properties. The properties examined here are stress, density and velocity profiles in the simulation region. To determine an average property, we divide the test region into a sufficient number of slices (for velocity and density profiles) or planes (for stress profiles). Then, we calculate the time averaged property for each slice or plane. For example, we add the x-component of the particle velocities in each slice and then we average over the number of particles in that slice at each time step. Finally, velocity profiles are obtained by computing the time average velocity for each slice during the simulation. Similar considerations are made for the density and stress profiles.

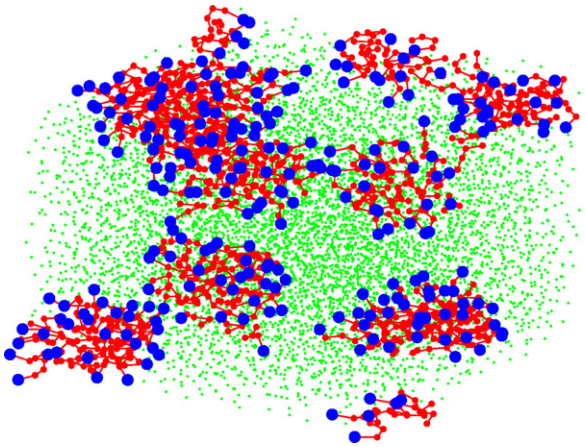

Fig. 3. Equilibrium configuration for a micellar concentration of 0.15. Green dashed dots represent the solvent; blue dots represent hydrophilic heads, and red dots represent hydrophobic tails. (For interpretation of the references to color in this figure legend, the reader is referred to the web version of the article.)

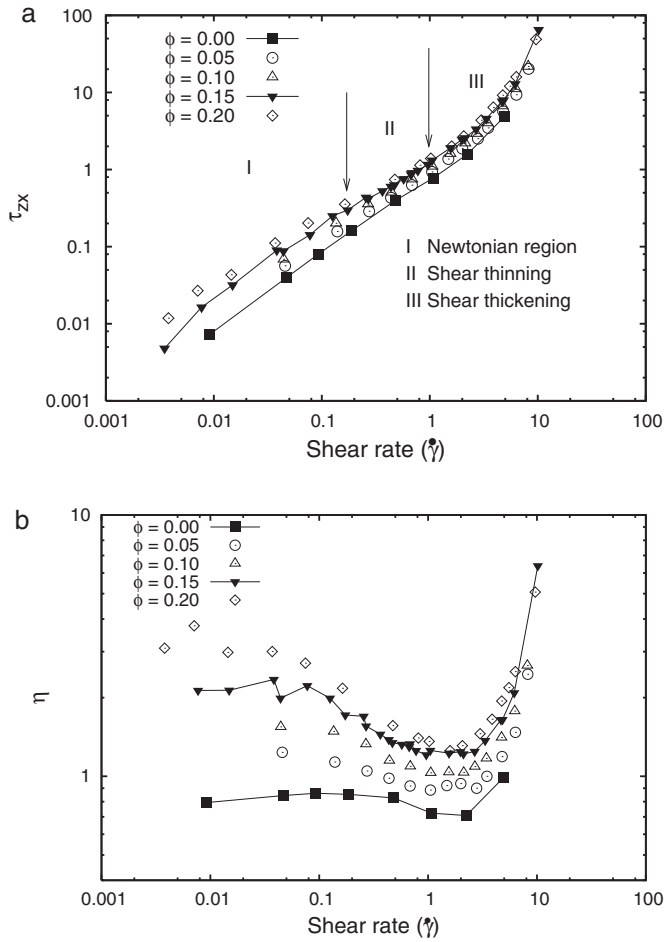

Fig. 4. Simple shear flow: (a) shear stress versus shear rate and (b) shear viscosity versus shear rate for various site concentrationsϕ.

4.1. Simple shear flow

4.1.1. Simple shear flow curves: stress versus shear rate and viscosity versus shear rate

The flow curves, τ_{zx} versus $\dot{\gamma}$, involve 100 planes x–y placed normal to the z axis, between the $z=0$ and $z=L_z$ surfaces. The stress $\tau_{zx}(z)$ and velocity profiles $v_x(z)$, are shown in Section 4.1.2. The shear stress τ_{zx} is the mean value of the $\tau_{zx}(z)$ profile, i.e., $\tau_{zx} = \sum_{i=1}^{Np} \tau_{zx,i}/Np$ where Np is the number of normal planes to the z axis. From the regression of the velocity profiles $v_x(z)$ the slope $\dot{\gamma}$ is found, corresponding to the imposed shear rate $\dot{\gamma}_{imp}$. With the mean stress τ_{zx} and shear rate $\dot{\gamma}$, corresponding to each $\dot{\gamma}_{imp}$, the shear viscosity η is obtained.

In Fig. 4a the shear stress τ_{zx} is plotted with the shear rate $\dot{\gamma}$ for the four concentrations analyzed here, including the solvent curve ($\phi=0$). Maintaining the velocity of the upper plate ($\dot{\gamma}_{imp}L_z$) constant, the resulting flow curve is monotonic and concentration dependent. Three flow regions are identified: the first region at small shear rates is Newtonian and extends up to a shear rate around 0.2. As the shear rate increases, the behavior of a second flow region is no longer Newtonian, but power-law, exhibiting shear-thinning between 0.2 and 1.0. For larger shear rates, a third region where shear-thickening is observed is located between 1.0 and 10. This flow curve is remarkably similar to that obtained by recent experimental data by Yamamoto et al. [58] using a solution of cetyltrimethylammonium bromide (CTAB) and sodium salicylate (NaSal) in the parallel plate geometry. Experimental flow curves exhibit a Newtonian region at low shear rates, followed by a region of slight shear-thinning and finally, a shear thickening behavior is observed at high shear rates.

The variation of the shear viscosity with shear rate is shown in Fig. 4b for same concentrations of Fig. 4a. The Newtonian and shear-thinning regions are followed by a quite wide shear-thickening region. The zero-shear-rate viscosity η_0 at low shear rates (0.005 and 0.1) is weakly dependent on concentration. Systems with 0.05 and 0.10 concentrations lie in the dilute regime, whereas those with larger concentrations (0.15 and 0.20) are found in the semi-dilute regime.

An interesting result of the simulations is the slight shear-thinning followed by an also slight shear thickening of the Lennard–Jones fluid (solvent). Despite the fact that in complex fluids the shear-induced molecular order or deformation produces shear-thinning, in Lennard–Jones fluids is not clear what produces such behavior, since the configuration analysis does not show any molecular ordering. Non-Newtonian behavior in simple fluids characterized by a Lennard–Jones fluid has been reported [59,60] using a "configurations thermostat" which does not exert additional constraints on the flow profiles. Results are in agreement with experiments on hard-sphere concentrated colloidal suspensions, namely, the Lennard–Jones fluid underwent shear-thinning for imposed shear rates lower than 7 and shear-thickening for larger shear rates. All these results seem to suggest than the L–J fluid is not particularly suitable to describe the rheological behavior of a Newtonian solvent. However, in the present work, we use this approximation on the basis that is a small contribution to the overall behavior of the system, and that the solvent is not responsible of the micelle ordering and deformation in the induction process of shear bands, as it is shown later.

4.1.2. Configurational analysis

Structural studies have related the three regions of the flow curve with structural changes in the internal state of the system. In equilibrium conditions the molecular structure corresponds to an isotropic or near-isotropic fluid, where a short-range ordering with characteristic length of 1σ and 2σ, becomes disordered for larger lengths, as seen in homogeneous isotropic fluids (see Fig. 3). In the Newtonian region, Fig. 5 shows the final configuration for a concentration of 0.15 at a shear rate of 0.04. The system has evolved from an equilibrium configuration (Fig. 3) with numerous micellar structures to a non-equilibrium structure (Fig. 5), *illustrating the interaction dynamics*. The final configuration of the system reveals that the surfactant molecules have formed a wormlike micelle *oriented in flow direction* (within the first region of the flow curve) and the solvent presents a random configuration at low shear rates. The internal structure of the micelle is preserved at this flow strength.

For second and third regions of the flow curve, final configurations of wormlike micelles ($\phi=0.15$) are depicted in Fig. 6(a–d) illustrating the spatial position of the micelles for increasing shear rates located in the shear-thinning region (Fig. 6a and,b) and in the shear-thickening region (Fig. 6c and d). The left hand-side pictures represent the velocity-gradient planes and the right hand-side pictures show the gradient-vorticity planes. In the shear-thinning region ($\dot{\gamma}=0.96$), the wormlike micelle observed in the Newtonian region (see Fig. 5) has been totally disrupted and single surfactant molecules migrate to the fixed surface, as shown in Fig. 6a. This distribution shows a band of molecules extending along the axial and neutral directions of the simulation region, normal to the gradient direction. The shear-thinning is apparently associated to the disruption of the wormlike micelles and to their further distribution in bands parallel to the flow direction. It is noticeable that in the depleted region most of the chains or agglomerates are disrupted, unlike in the low shear rate region where most of the micelles

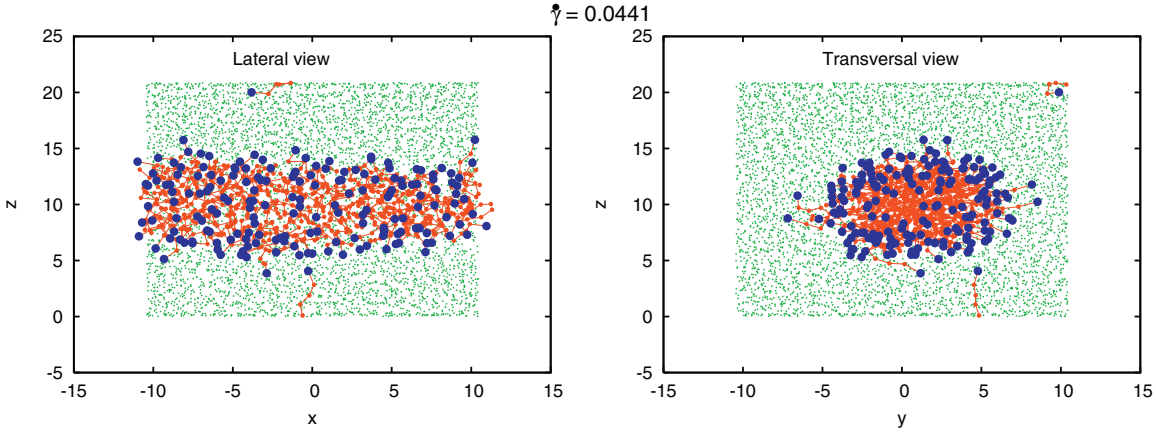

Fig. 5. Final configuration corresponding to the extreme of the Newtonian region for $\phi = 0.15$. Green dashed dots, blue dots and red dots represent the solvent, hydrophilic heads and hydrophobic tails, respectively. (For interpretation of the references to color in this figure legend, the reader is referred to the web version of the article.)

share agglomeration. Along the vorticity axis the same pattern prevails, indicating that the banding produced lies along the gradient direction (gradient banding) and not along the vorticity direction. To the end of the shear-thinning region, ($\dot{\gamma} = 1.98$), the band is fully extended axially and contracted in the vorticity direction (Fig. 6b). The banding produced along the gradient direction (left hand-side) where it is observed that the disrupted region at high shear rate is narrower than that of Fig. 6a, reflecting the growth of the agglomerate region. The drastic change in configuration arises along the vorticity direction (right hand-side). This drastic change in configuration suggests the initial stage of the diffusion of surfactant molecules to the negative y-direction and positive z-direction. Therefore, at this particular shear rate ($\dot{\gamma} = 1.98$), simultaneous gradient banding and banding along the vorticity direction ("vorticity banding") are predicted. This is precisely the transition point from banding along the gradient direction into banding along the vorticity direction.

It is important to mention that the orientation dynamics under flow in the shear-banding stage (in the plane of shear and along the vorticity direction) considering either the shear thickening or thinning response, is predicted in the semi-dilute regime. This dynamics can be accounted for by considering few cylindrical aggregates interacting with each other (growing or decreasing size) and orienting themselves under flow, producing migration and band formation. This is the situation that we are analyzing in the present work. Shear banding flow has been observed in many wormlike micellar systems in both the semi-dilute and concentrated regimes [61]. Moreover, giant micelles exhibit shear-thickening even in the dilute regime. In the present work, we are concerned with systems that may be governed by the interaction between micelles and orientation of the micellar aggregates under flow. Given the size of the system and the concentration regimes considered, here the dynamics of entanglement–disentanglement is not accounted for.

Along the shear-thickening region ($\dot{\gamma} = 3.34$), the diffusion process initiated at the end of the shear-thinning region terminates along the gradient direction. The molecules are distributed along a band extending axially and along the gradient direction, normal to the vorticity direction (Fig. 6c). The entanglement region has grown substantially, covering almost the entire flow region. Upon increasing the shear rate to $\dot{\gamma} = 4.82$, the system exhibits two bands normal to the vorticity direction, where the largest magnitude of shear-thickening is observed. Final configurations suggest that these bands are due to a diffusion process along the vorticity direction. Finally, Fig. 7(a–d) depicts the effect of concentration in the formation of bands along the vorticity direction, all figures in the shear thickening region. In Fig. 7a, the solvent alone exhibits an isotropic behavior. As the concentration increases, bands are formed. However, it is clear that the formation of these bands requires a minimum value of the concentration, in this case, larger than 0.1, as shown in Fig. 7c and d.

Shear banding along the vorticity direction has been reported by Fischer et al. [26] in the aqueous surfactant solution of cetylpyridinium chloride and sodium salicylate, investigated in a transparent strain-controlled Taylor Couette flow cell. This particular wormlike micellar solution exhibits shear thinning at low shear rates and subsequently, shear thickening at high shear rates. Once the shear-thickening regime is reached, a transient phase separation of the solution into turbid and clear ring-like patterns oriented perpendicular to the vorticity axis are observed. These patterns are consequences of the structural changes of the oriented micellar aggregates and can be explained molecularly, to our knowledge for the first time, in the context of the present molecular model.

The predictions of the present model are in agreement with other analyses that predict van der Waals loops in the stress, so both gradient and vorticity banding can occur [29,62]. But in contrast to these analyses, the prediction of banding normal to the vorticity direction was made here without the condition of multi-valued flow curve.

Recent research on banding normal to the vorticity axis relates it with the occurrence of normal stresses along the gradient direction in polymer systems. The non-uniform stretching of polymer chains gives rise to normal stresses directed toward the moving surface. When these stresses are sufficiently large, they can generate a flow along the gradient direction. Under steady-state this motion gives rise to bands that are in internal rolling motion [25]. In the case of wormlike micelles, the non-uniform elastic deformation of the in-homogeneities (in this case the non-uniform distribution of micellar entanglement state and deformation) gives rise to hoop stresses that can generate the rolling motion of the bands. Alternatively, normal stresses giving rise to vorticity banding can be generated within the interface of the gradient banded structure. In this case, initially a gradient banding structure develops, which is then followed by the formation of vorticity bands [32]. This is precisely what is observed in Fig. 6(a–d). The in-homogeneities in the stretching of the micelles give rise to normal stresses pointing toward the moving surface (see the left-hand side of Fig. 6). The diffusion of micelles in the gradient direction reflects the flow along this direction for increasing shear rates; until the entire flow cell is covered by agglomerated micelles in the shear-thickening regime (see Fig. 6d). The diffusion process may generate normal stresses along the gradient axis giving rise to the rolling motion

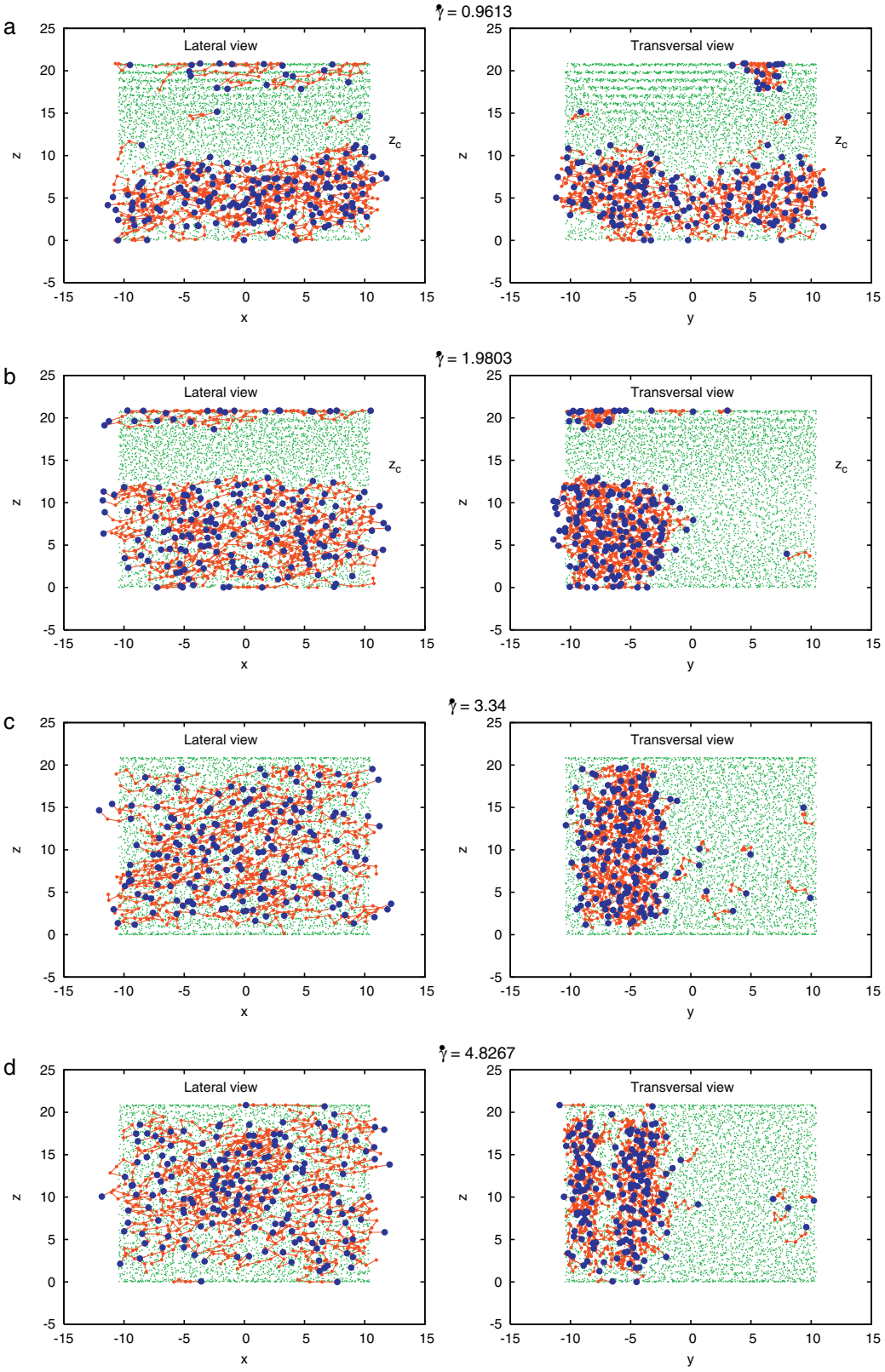

Fig. 6. Lateral and transversal views of the final configuration in: (a and b) the shear-thinning region and (c and d) shear-thickening region for $\phi = 0.15$.

and band formation normal to the vorticity axis, as seen in the right-hand side of Fig. 6d. This behavior is analyzed in a forthcoming publication on predictions of the normal stresses on the surfaces.

4.1.3. Density and velocity profiles

With the final configurations described in the previous section, the relationship between the velocity and stress fields is analyzed. To obtain the density profiles $\rho(z)$ and velocity profiles $v_x(z)$, 100

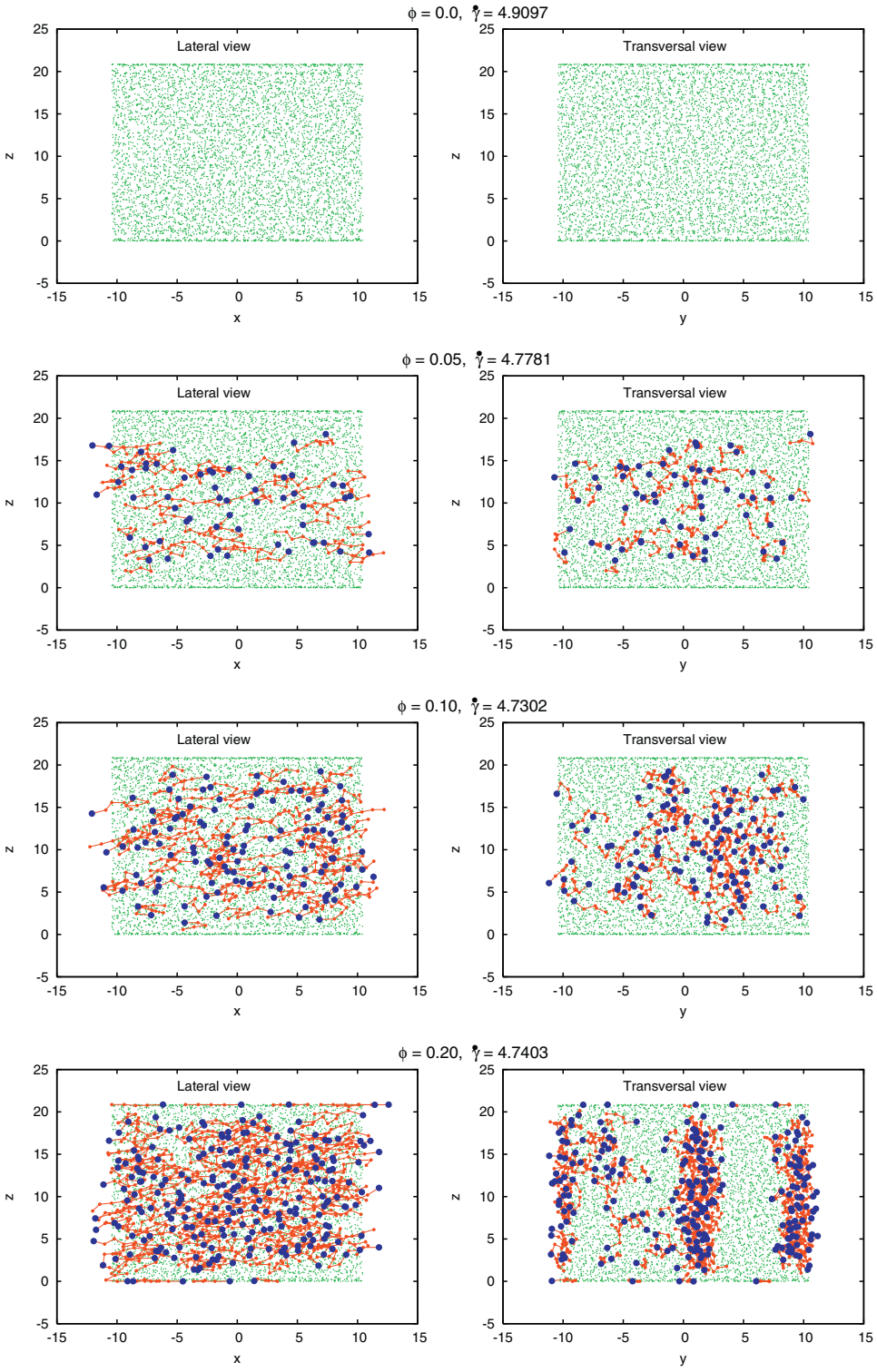

Fig. 7. Effect of concentration on the formation of "vorticity banding": (a–c) dilute regime, and (d) semi dilute regime.

$x-y$ planes are placed normal to the z axis, between $z=0$ and $z=L_z$. In Fig. 8, the density is plotted as a function of the confining distance for a concentration of 0.15. In the Newtonian region ($\dot{\gamma}=0.0035$), the density profile is symmetric, exhibiting a slight layer ordering due to the surface. Along the second flow region ($0.57<\dot{\gamma}<0.96$) the density profile between the plates is now asymmetric, revealing large fluctuations next to the moving wall (right). These oscillations are associated to a slight ordering that the solvent exhibits next to the moving wall (see Fig. 6a). Along this flow regime, the fluid is distributed in two regions, one of low density next to the fixed wall and another one with high density next to the moving surface. Similar behavior is observed at other concentrations. Finally, along the shear-thickening region ($3.34<\dot{\gamma}<6.17$) density profiles are again symmetric.

Velocity profiles corresponding to the three regions of flow behavior are shown in Fig. 9(a, b and c, respectively). In the Newto-

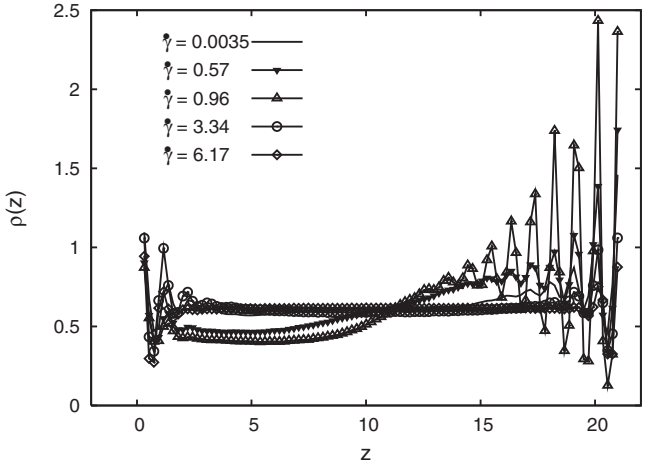

Fig. 8. Density profiles $\rho(z)$ with concentration of 0.15, for various shear rates under simple shear flow.

nian region at low shear rates, the velocity profiles are straight lines within 0.0035 and 0.038 of shear rate. In the shear-thinning region we observe a continuous development of two shear bands as the shear rate increases, whose slopes are indicated in Fig. 9b. The larger shear rate corresponds to that near the fixed wall. Finally, along the shear-thickening region, the velocity profiles become linear again, even for the largest value (6.17). Some experimental results reveal that under gradient banding, the largest velocity gradient is located near the moving wall. However, results here presented indicate that the lower velocity gradient band is located next to the moving wall. These velocity profiles are qualitatively consistent with those obtained by Yamamoto et al. [58] for shear-thickening fluids. In fact, in these fluids, it is observed that a highly viscous structured oriented region forms near the moving wall, generating a low shear rate layer. The behavior of the velocity profiles is given particular attention in a forthcoming publication.

It is possible to establish a relationship between the density and velocity profiles. When the density profile is symmetric, the velocity profile is almost linear. Non-homogeneous density profiles derive from the shear-induced molecular organization. Along the Newtonian region, the fluid is isotropic, the velocity profile is linear and the density profile is symmetric. In the shear-thickening region, ($\dot{\gamma} \approx 4.8$), the fluid is isotropic again for the lower concentrations (0.0, 0.05 and 0.10, see Fig. 7a–c) and band formation normal to the vorticity axis for ϕ of 0.15 (Fig. 6d) and 0.20 (Fig. 7d). As these bands extend along the gradient axis, the velocity profile is linear and the density profile is symmetric. However, along the shear-thinning section, the lower density region possesses larger velocity gradients, while the region with higher density corresponds to the lower velocity gradients. Due to this density differences, it is likely that the fluid band normal to the gradient axis is associated to a diffusion process from the high density region to the low density domain.

4.1.4. Stress profiles

The stress profiles along the flow cell perpendicular to the flow direction are shown in Fig. 10a and b. In Fig. 10a, for shear rates located in the Newtonian region (0.0035 and 0.04) the stress is almost constant. As the shear rate increases within the shear-thinning region, the two-band structure is reflected in a low and high stress profiles. The larger stress corresponds to the high shear rate band (see Fig. 9b) followed by a smooth transition to the low stress value corresponding to the low shear rate band. This is clearly depicted in the stress curves for shear rates of 0.77 and 0.96. The higher stress value is associated to those sections of the simulation domain where the density of surfactant molecules is larger. In Fig. 9b, the inflection point of the velocity is located approximately at $z = 12$ (close to the center of the flow cell). This inflection point is associated to the fluid band normal to the gradient direction. The change in the peak stress from 1.5 to approximately 1.0 is also located at this point. Under homogeneous simple shear flow, the stress is constant across the gap between the moving and stationary plates, but under banding flow, the stress is constant within each band. The average stress is calculated by averaging the stress profile across the gap, and it coincides with the experimental torque measurements. It turns out that in the banding flow region, the spatially resolved stress may change from one value into another one across

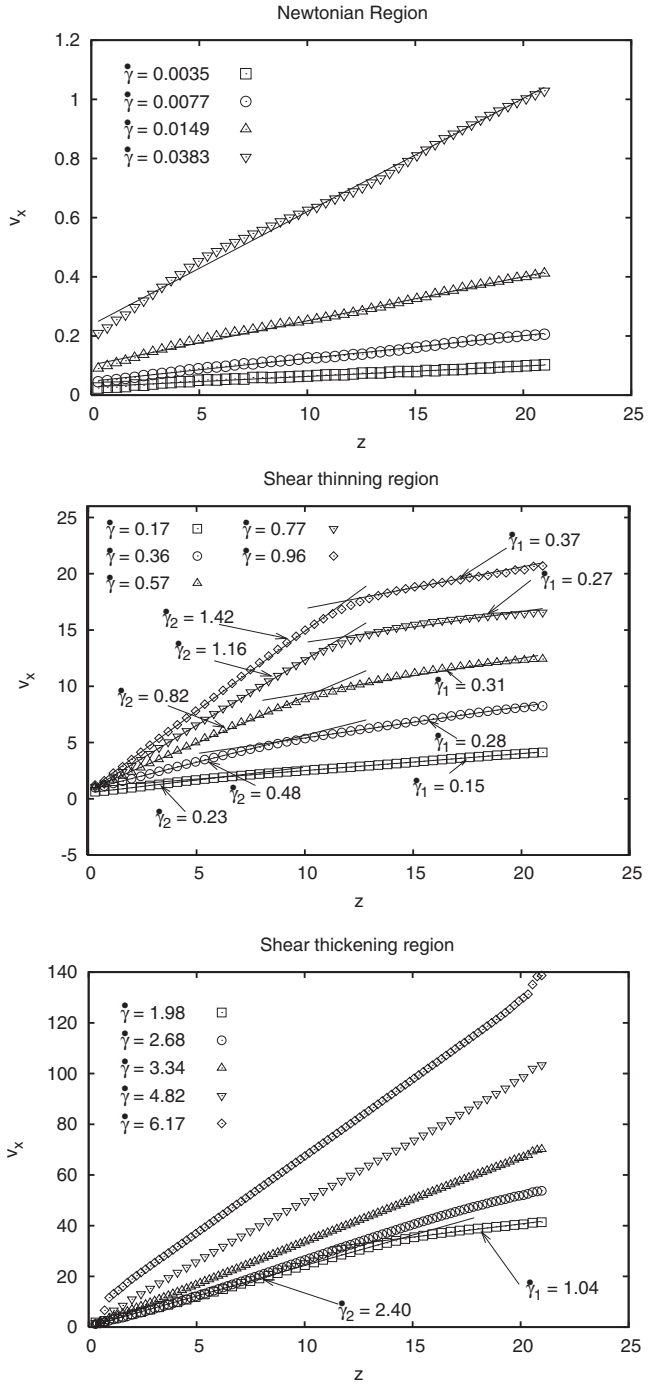

Fig. 9. Velocity profiles $v_x(z)$ corresponding to the indicated flow regimes under simple shear for a concentration of 0.15.

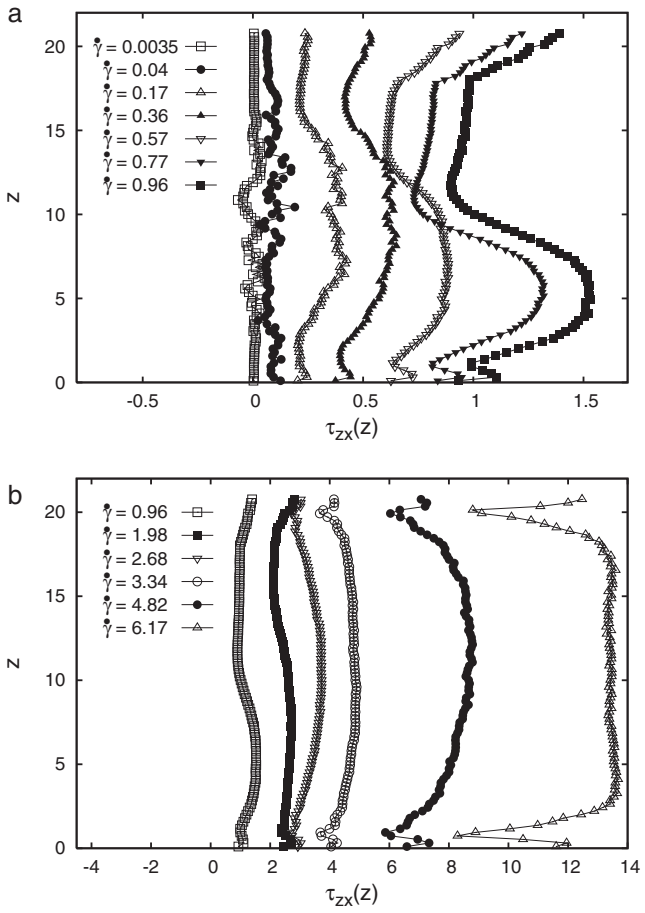

Fig. 10. Shear stress profiles τ_{zx} along the gradient axis z for a concentration of 0.15. (a) Newtonian and shear-thinning regions. (b) Shear-thickening region.

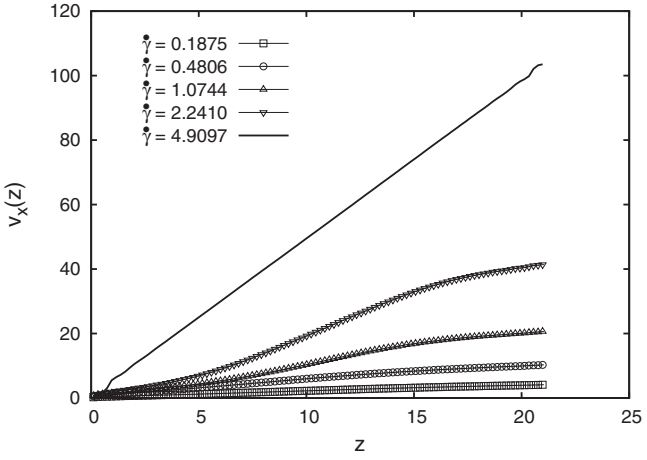

Fig. 11. Velocity profiles $v_x(z)$ for the Lennard–Jones fluid ($\phi = 0.0$) under simple shear flow.

the interface, consistent with the change in velocity profile at this point (see Figs. 9 and 10b and a). This is experimentally observed as a change in spatially resolved birefringence at the interface (see Ref. [63]) as one goes from a less-ordered structure into a more oriented one). In the region where the shear-thickening occurs, Fig. 10b, the development of the stress profile for increasing shear rates across the flow cell is more drastic in magnitude and attains an almost flat profile at very high shear rates (6.17). There is, however, a low stress region next to the walls, reminiscent of a stress boundary layer.

4.1.5. Density and velocity profiles: Lennard–Jones fluid

As mentioned in Section 4.1.1, the motion of particles modeled with a Lennard–Jones potential simulating a solvent is discussed. Some works have reported a non-Newtonian behavior with this fluid. Heyes [64] reports flow curves for various densities and temperatures. For example, at a reduced density of 0.8 and reduced temperature of 1.86, this fluid shows a slight shear-thinning between shear rates of 0.1 and 1.0. Increasing density with decreasing temperature, shear-thinning appears at lower shear rates. Other works [65] associated the shear-thinning to a flow-induced ordering. Evans and Morriss [66] established that this ordering is due to the assumed velocity profile of the thermostat to hold a constant temperature. Thereafter, Refs. [59,60] verified these results, and suggested that the molecular ordering is associated to a thermostat artifact even though the fluid experiences shear-thinning followed by shear-thickening between $1 \leq \dot\gamma \leq 10$, near the triple point conditions.

It is important to establish that this non-Newtonian behavior in the solvent particle used here (without ordering) contributes little to the *molecular deformation* and *bands* generated by the micellar solution. In this work, the Nose–Hoover thermostat is used to maintain a constant temperature but this thermostat is applied only to those components of the velocity vector which develop a peculiar velocity. With this consideration, the final configuration does not exhibit any ordering molecular in the shear thickening region. For example, for a shear rate of 4.91 (Fig. 7a), the final configuration exhibits a random and isotropic organization with the absence of ordering molecular. For similar shear rates, Delhommelle et al. [59] report a molecular ordering of the fluid (using a PBT thermostat) which vanishes when a configurational thermostat is used. The configurational thermostat does not require the assumption of the velocity profile to maintain a constant temperature. In this work, we do not use a configurational thermostat but it is demonstrated that if the Nose-Hoover thermostat is applied only to those components of the velocity which develop a peculiar velocity, no ordering in the shear-thinning and shear thickening regions is predicted for the L–J fluid.

In Fig. 11, the velocity profiles $v_x(z)$ are presented for the L–J fluid. In the Newtonian region ($\dot\gamma = 0.18$) and shear-thickening region ($\dot\gamma = 4.9$) linear velocity profiles are observed. However, in the shear-thinning region ($\dot\gamma$ of 1.07 and 2.24), three regions of different shear rates are predicted. Next to the boundaries, the shear rate is lower than that in the central region, where the fluid has a higher velocity gradient. The central region corresponding to high velocity gradient, presents a lower density (not shown). Apparently, non-homogeneous density profiles are related to distinct velocity gradients. It is important to mention that the density profile of the solvent is different to that observed in the micellar solutions, from which differences in the velocity profiles appear. For similar shear rates from 0.96 and 1.98 (Fig. 9b), the system with 0.15 concentration exhibits two regions with different velocity gradient, where the fluid exhibits *gradient-banding,* being independent of the rheological behavior of the solvent.

4.2. Poiseuille's flow

This flow is generated between two fixed surfaces by means of the applied external force F_e along the x direction. Under F_e, the fluid moves along the x axis, with the gradient direction z and vorticity direction y. The velocity $v_x(z)$ and stress profiles $\tau_{zx}(z)$, follow same conditions of the simple shear flow. Flow curves display the relation between τ_w and $\dot\gamma_w$, where τ_w is the shear stress $\tau_{zx}(z = \pm 0.5L_z)$ eval-

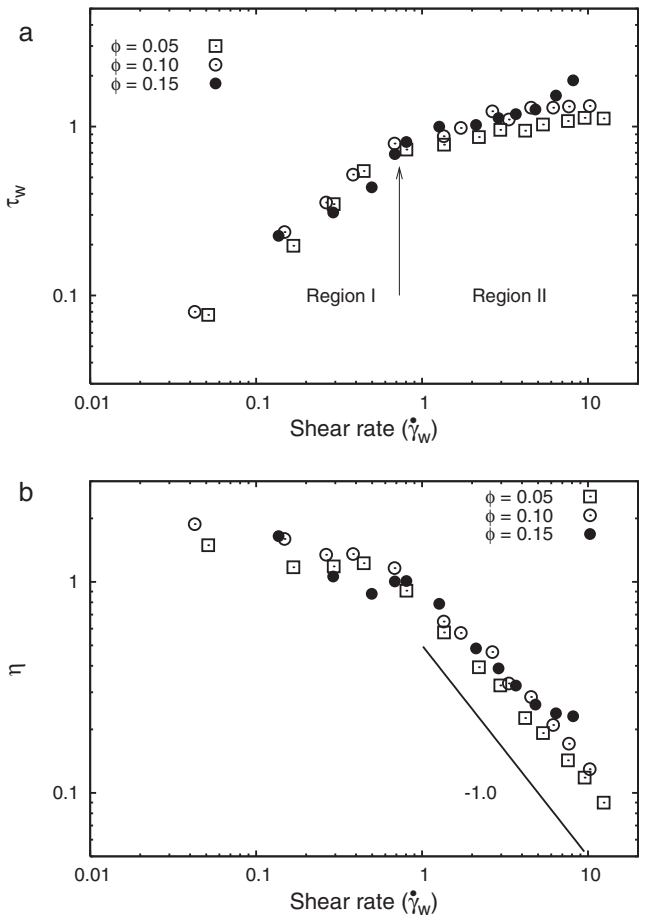

Fig. 12. Poiseuille's flow. (a) Wall stress and (b) shear viscosity as functions of shear rate $\dot{\gamma}_w$ for various site concentrations.

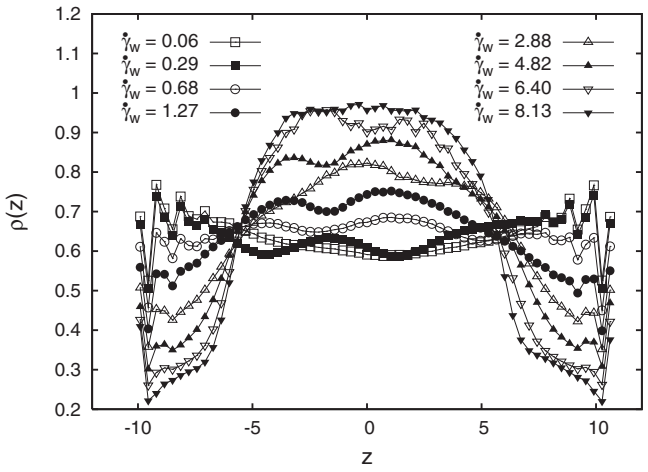

Fig. 13. Poiseuille's flow. Density profiles $\rho(z)$ along the gradient direction z for a site concentration of 0.15.

uated on the walls. Similarly, $\dot{\gamma}_w$ is the local shear rate obtained from the velocity profile and evaluated on the walls $\dot{\gamma}_w = dv_x/dz|_{z=0.5L_z}$.

In Fig. 12a the stress at the wall τ_w is plotted with shear rate $\dot{\gamma}_w$ for three concentrations (0.05, 0.10 and 0.15) and in Fig. 12b the viscosity is plotted with shear rate. There are two regions of flow behavior: in region 1, a near-Newtonian behavior is observed followed by a shear-thinning region for shear rates larger than approximately 0.7. The shear-thinning is pronounced (slope of −0.83), although it does not approach the slope of −1 corresponding to the plateau. The smaller concentrations flow curves go into a near-plateau in region II, whereas the flow curve with concentration of 0.15 begins to approach a second Newtonian region at the highest shear rate. In contrast to the simple shear flow curves, in this case the shear-thickening behavior is not observed in the ranges of the imposed external force (pressure gradient) and concentrations considered.

Fig. 13 depicts the density profiles in the radial direction (z) for concentration of 0.15. In the Newtonian region ($\dot{\gamma}_w$ of 0.06, 0.29 and 0.68), the density profile is almost symmetric with slight waves in the central region and some peaks next to the walls. The waves are due to the micellar structures which preserve the flow conditions and the peaks are due to a banding characteristic of ordering fluids. In the shear-thinning region ($\dot{\gamma}_w \geq 1.27$), for increasing $\dot{\gamma}_w$, the system density increases toward the center of the flow region and diminishes next to the walls. Again, two regions of different density are shown in the curve. The region next to the walls where the density is low spans almost half a radius distance from the walls. As expected, the micelles tend to migrate to the central regions of the pipe where the shear rate is small and this effect is more pronounced as the shear rate increases. This growth of the "slip layer" with shear rate is remarkable.

In Fig. 14, the velocity profiles $v_x(z)$ in (a) Newtonian region and (b) shear-thinning region are presented. In the Newtonian region (Fig. 14a), velocity profiles are parabolic centered, with a maximum velocity located at the pipe center ($z = 0$). For the range $0.13 \leq \dot{\gamma}_w \leq 0.68$, the fluid exhibits some slipping on the surface. Increasing the shear rate (Fig. 14b) and in the shear-thinning region, the velocity profile tends to a plug-flow profile. Notice that the flat profile section corresponds to the region where the larger density

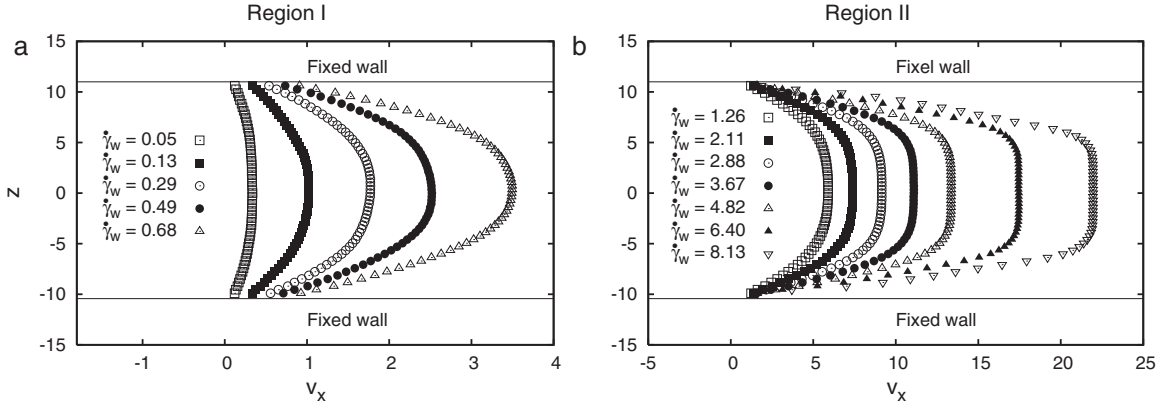

Fig. 14. Poiseuille's flow. Velocity profiles $v_x(z)$ for a site concentration of 0.15, in the (a) Newtonian and (b) shear-thinning regions.

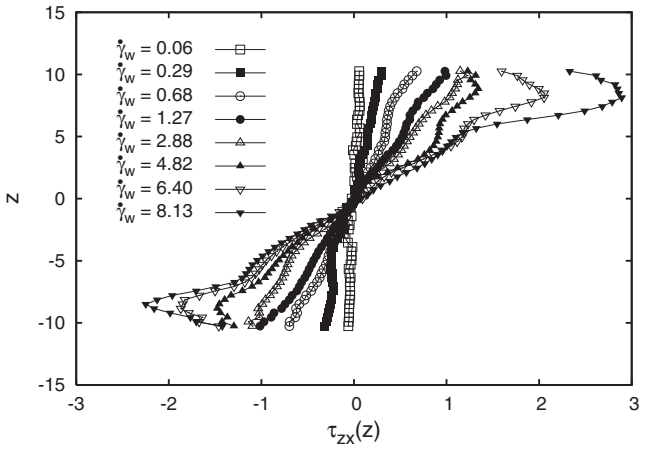

Fig. 15. Poiseuille's flow. Shear stress profiles $\tau_{zx}(z)$ along the gradient direction z for a site concentration of 0.15.

is found (see Fig. 13) and the "slip layer" where density is low, corresponds to an almost linear velocity profile spanning almost half a radius distance from the wall.

The stress profiles for the wall shear rates considered are plotted in Fig. 15. For low wall shear rates, the profile is linear in accordance to Newtonian behavior. As the wall shear rate increases, the region next to the walls begins to present a reversal in the stress values and deviations from the linear profile, becoming more noticeable for the largest shear rates. This "stress boundary layer" is maybe attributed to the depletion of micelles in regions next to the wall. When the plug flow profile develops, the shear stress is zero in this region, and nearly constant for the almost linear velocity profile. These predictions indicate that the reversal to low values of the stress next to the walls corresponds to an inflection in the density profiles (see Fig. 13) along this region. It also shows that the "stress boundary layer" does not coincide with the velocity boundary layer or "slip layer".

In the Newtonian region, we observe clusters of micelles in the central region or next to the walls that are not greatly deformed (not shown). But, in the shear thinning region, as the shear rate increases, there is an uneven distribution of micellar clusters next to the walls, and for higher shear rates the micellar distribution in this region tend to be uniform. In Fig. 16, the final configuration is presented for $\phi = 0.15$, with shear rate of 2.88. The molecular organization of the system exhibits a small deformation of the wormlike micelle at the central region of the pipe, that contrasts with low agglomeration of the deformed clusters next to the walls.

These predictions of the molecular model presented so far are in agreement with recent experiments and predictions worked out by Yamamoto et al. [23]. The flow curve for a micellar solution of CTAB/NaSal (cetyltrimethylammonium bromide with sodium salicylate) used by these authors is similar to that shown in Fig. 12. Predictions of the velocity profiles using the MBM model are also in agreement with those presented in Fig. 14. Furthermore, the behavior of the shear stress next to the wall is remarkably similar to that shown in Fig. 15, where a maximum followed by a decreasing stress next to the wall is predicted. Finally, experiments on flow visualization performed by the referred paper show regions of turbidity associated to a structure, whose size is comparable to the wave length of light, is formed and scatters the impinging light. These layers of turbidity lie almost parallel next to the wall, growing toward the channel center with increasing wall shear rate. This is precisely what is observed in the simulations presented in Fig. 16.

5. Concluding remarks

One of the main contributions of this work is to establish a relationship between molecular structure and spatial configuration with transport properties of a complex system undergoing simple shear flow. At low shear rates the stress is linear with the shear rate and the conformation of the system is isotropic, the micelle preserving its equilibrium conformation and the solvent is in random state.

A second flow region is located at higher shear rates, where shear thinning manifests, revealing the formation of bands positioned normal to the gradient direction (gradient banding). Experimentally, to attain stability along this flow region, the flow becomes inhomogeneous and separates in bands of different shear rates. A substantial change of the molecular structure of the solution occurs, where the equilibrium structure of the micelles has been profoundly modified. In this region, non-homogeneous density profiles derive from the shear-induced molecular organization.

A third region of flow behavior is found at large shear rates, where the system exhibits shear thickening. Along the gradient direction, the micelles interact without the presence of shear bands, corresponding to linear velocity profiles. Also along this region, the generation of bands positioned perpendicular to the vorticity axis is predicted. In summary, a wormlike chain or micelle is predicted in the equilibrium state. Molecular interactions are strongly modified by the flow, inducing deformation and orientation of the micelle.

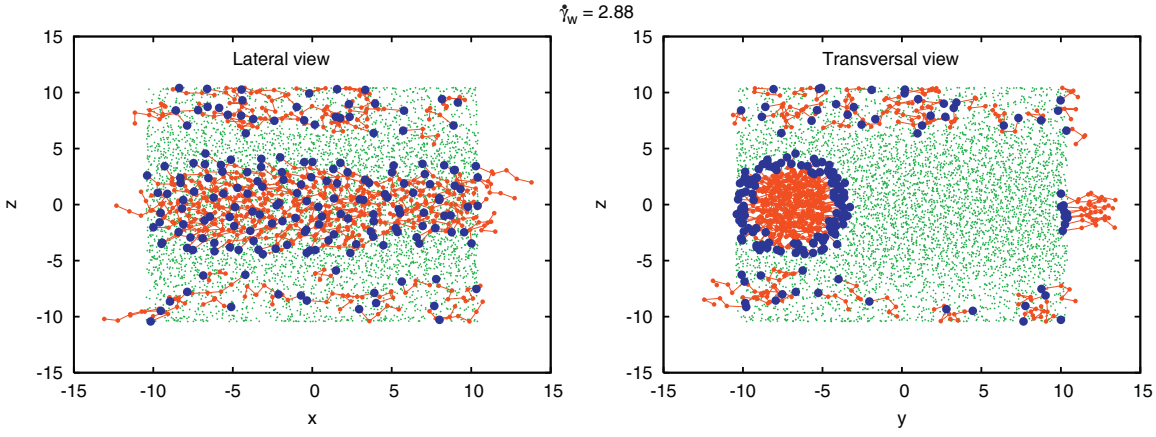

Fig. 16. Poiseuille's flow. Lateral and transversal views of the final configuration in the region of strong shear-thinning, $\phi = 0.15$. Green dashed dots, blue dots and red dots represent the solvent, hydrophilic heads and hydrophobic tails, respectively. (For interpretation of the references to color in this figure legend, the reader is referred to the web version of the article.)

The overall predictions of the present model are in agreement with theoretical analyses that predict gradient banding followed by vorticity banding as the fluid shear-thickens. Also, they agree with the assumption related to the contribution of normal stresses in the generation of the bands normal to the vorticity axis. Furthermore, agreement is also found with experiments performed in a wormlike micellar solution, where bands perpendicular to the vorticity axis are observed in a Couette cell, simultaneously to the apparition of the shear-thickening behavior. In Poiseuille's flow, the appearance of an oriented band next to the walls with lower density causes a deviation in this region, from the expected linear profile for pipe flow (see Figs. 13, 14b and 15) into a two-banded stress profile. This is also experimentally observed in the birefringence patterns (see Ref. [23]). Moreover, theoretical and experimental agreement is found in Poiseuille's flow with other works reported in the current literature. This is a novel contribution toward the understanding of complex flow behavior.

Acknowledgements

The authors are grateful for the financial support from the National Council for Science and Technology (CONACYT) through the projects 83501 and 100195.

References

[1] M.E. Cates, S.J. Candau, Statics and dynamics of worm-like micelles, J. Phys. Condens. Matter 2 (1990) 6869–6892.
[2] J.N. Israelachvili, Intermolecular and Surface Forces, Academic Press, San Diego, 1991.
[3] J.F. Berret, Transient rheology of wormlike micelles, Langmuir 13 (1997) 2227–2234.
[4] J.F.A. Soltero, F. Bautista, J.E. Puig, O. Manero, Rheology of cetyltrimethylammonium p-toluenesulfonate-water system. 3. Nonlinear viscoelasticity, Langmuir 15 (1999) 1604–1612.
[5] J.F.A. Soltero, F. Bautista, E. Pecina, J.E. Puig, O. Manero, Z. Proverbio, P.C. Schulz, Rheological behavior in the didodecyldimethylammonium bromide/water system, Colloid Polym. Sci. 278 (2000) 37–47.
[6] H. Rehage, H. Hoffmann, Viscoelastic surfactant solutions: model systems for rheological research, Mol. Phys. 74 (1991) 933–973.
[7] P.D. Olmsted, O. Radulescu, C.-Y. Lu, Johnson–Segalman model with a diffusion term in cylindrical Couette flow, J. Rheol. 44 (2000) 257–275.
[8] H. Rehage, H. Hoffmann, Rheological properties of viscoelastic surfactant systems, J. Phys. Chem. 92 (1988) 4712–4719.
[9] J.F. Berret, D.C. Roux, G. Porte, Isotropic-to-nematic transition in wormlike micelles under shear, J. Phys. II 4 (1994) 1261–1279.
[10] J.F. Berret, G. Porte, J.P. Decruppe, Inhomogeneous shear flows of wormlike micelles. A master dynamics phase diagram, Phys. Rev. E 55 (1997) 1668–1676.
[11] C. Grand, J. Arrault, M.E. Cates, Slow transients and metastability in wormlike micelle rheology, J. Phys. II 7 (1997) 1071–1086.
[12] V. Schmitt, F. Lequex, A. Pousse, D. Roux, Flow behavior and shear induced transition near an isotropic/nematic transition in equilibrium polymers, Langmuir 10 (1994) 955–961.
[13] P.T. Callaghan, M.E. Cates, C.J. Rofe, J.B.A.F. Smeulders, A study of the "Spurt Effect" in wormlike micelles using nuclear magnetic resonance microscopy, J. Phys. II 6 (1996) 375–393.
[14] R.W. Mair, P.T. Callaghan, Observation of shear banding in worm-like micelles by NMR velocity imaging, Europhys. Lett. 36 (1996) 719–724.
[15] M.M. Britton, P.T. Callaghan, Two-phase shear band structure at uniform stress, Phys. Rev. Lett. 78 (1997) 4930–4933.
[16] R.W. Mair, P.T. Callaghan, Shear flow of wormlike micelles in pipe and cylindrical Couette geometries as studied by nuclear magnetic resonance microscopy, J. Rheol. 41 (1997) 901–924.
[17] J.-B. Salmon, A. Colin, S. Manneville, F. Molino, Velocity profiles in shear banding wormlike micelles, Phys. Rev. Lett. 90 (2003) 228303:1–228303:4.
[18] S. Manneville, Recent experimental probes of shear banding, Rheol. Acta 47 (2008) 301–318.
[19] L. Bécu, D. Anache, S. Manneville, A. Colin, Evidence for three dimensional unstable flows in shear banding wormlike micelles, Phys. Rev. E 76 (2007) 011503:1–011503:12.
[20] M.P. Lettinga, S. Manneville, Competition between shear banding and wall slip in wormlike micelles, Phys. Rev. Lett. 103 (2009) 248302:1–248302:4.
[21] S. Manneville, A. Colin, G. Waton, F. Schosseler, Wall slip, shear banding, and instability in the flow of a triblock copolymer micellar solution, Phys. Rev. E 75 (2007) 061502:1–061502:10.
[22] J.M. Adams, S.M. Fielding, P.D. Olmsted, The interplay between boundary conditions and flow geometries in shear banding: hysteresis, band configurations, and surface transitions, J. Non-Newtonian Fluid Mech. 151 (2008) 101–118.
[23] T. Yamamoto, T. Hashimoto, A. Yamashita, Flow analysis for wormlike micellar solutions in an axisymmetric capillary channel, Rheol. Acta 47 (2008) 963–974.
[24] S.M. Fielding, H.J. Wilson, Shear banding and interfacial instability in planar Poiseuille flow, J. Non-Newtonian Fluid Mech. 165 (2010) 196–202.
[25] J.K.G. Dhont, W.J. Briels, Gradient and vorticity banding, Rheol. Acta 47 (2008) 257–281.
[26] P. Fischer, E.K. Wheeler, G.G. Fuller, Shear-banding structure orientated in the vorticity direction observed for equimolar micellar solution, Rheol. Acta 41 (2002) 35–44.
[27] V. Herle, P. Fischer, E.J. Windhab, Stress driven shear bands and the effect of confinement on their structures—A rheological, flow visualization, and rheo-SALS study, Langmuir 21 (2005) 9051–9057.
[28] V. Herle, J. Kohlbrecher, B. Pfister, P. Fischer, E.J. Windhab, Alternating vorticity banding in a solution of wormlike micelles, Phys. Rev. Lett. 99 (2007) 1–4, 158302.
[29] L.B. Chen, C.F. Zukoski, B.J. Ackerson, H.J.M. Hanley, G.C. Straty, J. Barker, C.J. Glinka, Structural changes and orientational order in a sheared colloidal suspension, Phys. Rev. Lett. 69 (1992) 688–691.
[30] J.K.G. Dhont, M.P. Lettinga, Z. Dogic, T.A.J. Lenstra, H. Wang, S. Rathgeber, P. Carletto, L. Willner, H. Frielinghaus, P. Lindner, Shear banding and microstructure of colloids in shear flow, Faraday Discuss. 123 (2003) 157–172.
[31] K. Kang, M.P. Lettinga, Z. Dogic, J.K.G. Dhont, Vorticity banding in rodlike virus suspension, Phys. Rev. E 74 (2006) 1–12, 026307.
[32] S.M. Fielding, Vorticity structuring and velocity rolls triggered by gradient shear bands, Phys. Rev. E 76 (2007) 016311:1–016311:8.
[33] A. Jabbarzadeh, J.D. Atkinson, R.I. Tanner, Effect of molecular shape on rheological properties in molecular dynamics simulation of StarHComb, and linear polymer melts, Macromolecules 36 (2003) 5020–5031.
[34] J.D. Moore, S.T. Cui, H.D. Cochran, P.T. Cummings, A molecular dynamics study of a short-chain polyethylene melt. I. Steady state shear, J. Non-Newtonian Fluid Mech. 93 (2000) 83–99.
[35] J.D. Moore, S.T. Cui, H.D. Cochran, P.T. Cummings, A molecular dynamics study of a short-chain polyethylene melt. II. Transient response upon onset of shear, J. Non-Newtonian Fluid Mech. 93 (2000) 101–116.
[36] Z. Xu, J.J. de Pablo, S. Kim, Transport properties of polymer melts from nonequilibrium molecular dynamics, J. Chem. Phys. 102 (1995) 5836–5844.
[37] J. Castillo-Tejas, J.F.J. Alvarado, G. González-Alatorre, G. Luna-Barcenas, I.C. Sanchez, R. Macias-Salinas, O. Manero, Nonequilibrium molecular dynamics simulations of rheological and structural properties of linear and branched molecules simple shear and Poiseuille flow, instabilities and slip, J. Chem. Phys. 123 (2005) 1–15, 054907.
[38] R. Khare, J.J. de Pablo, Rheological, thermodynamic, and structural studies of linear and branched alkanes under shear, J. Chem. Phys. 107 (1997) 6956–6964.
[39] M. Stevens, M. Mondello, G.S. Grest, S.T. Cui, H.D. Cochran, P.T. Cummings, Comparison of shear flow of hexadecane in a confined geometry and in bulk, J. Chem. Phys. 106 (1997) 7303–7314.
[40] C.J. Mundy, J. Siepmann, M.L. Klein, Decane under shear: a molecular dynamics study using reversible NVT-SLLOD and NPT-SLLOD algorithms, J. Chem. Phys. 103 (1995) 10192–10200.
[41] M. Kröguer, W. Loose, S. Hess, Rheology and structural changes of polymer melts via non equilibrium molecular dynamics, J. Rheol. 37 (1993) 1057–1079.
[42] H.M. Laun, R. Bung, S. Hess, W. Loose, O. Hess, K. Hahn, E. Hädicke, R. Hingmann, F. Schmidt, P. Lindner, Rheological and small angle neutron scattering investigation of shear-induced particle structures of concentrated polymer dispersions submitted to plane Poiseuille and Couette flow, J. Rheol. 36 (1992) 743–787.
[43] M. Kröger, R. Makhloufi, Wormlike micelles under shear flow: a microscopic model studied by nonequilibrium molecular dynamics computer simulations, Phys. Rev. E 53 (1996) 2531–2536.
[44] J.T. Padding, E.S. Boek, Influence of shear flow on the formation of rings in wormlike micelles: a nonequilibrium molecular dynamics study, Phys. Rev. E 70 (2004) 1–10, 031502.
[45] J.T. Padding, E.S. Boek, W.J. Briels, Rheology of wormlike micellar fluids from Brownian and molecular dynamics simulations, J. Phys. Condens. Matter 17 (2005) S3347.
[46] R. Goetz, R. Lipowski, Computer simulations of bilayer membranes: self-assembly and interfacial tension, J. Chem. Phys. 108 (1998) 7397–7409.
[47] W.K. den Otter, S.A. Shkulipa, W.J. Briels, Buckling and persistence length of an amphiphilic worm from molecular dynamics simulations, J. Chem. Phys. 119 (2003) 2363–2368.
[48] W.J. Briels, P. Mulder, W.K. den Otter, Simulations of elementary processes in entangled wormlike micelles under tension: a kinetic pathway to Y-junctions and shear induced structures, J. Phys. Condens. Matter 16 (2004) S3965.
[49] G.J. Martyna, M.E. Tuckerman, D.J. Tobias, M.L. Klein, Explicit reversible integrators for extended system dynamics, Mol. Phys. 87 (1996) 1117–1157.
[50] J.A. Pryde, The Liquid State, Hutchinson University Library, London, 1969.
[51] M.P. Allen, D.J. Tildesley, Computer Simulation of Liquids, Clarendon Press, Oxford, 1987.
[52] R.G. Larson, The Structure and Rheology of Complex Fluids, Oxford University Press, 1999.
[53] J. Appell, G. Porte, Polymer like behaviour of giant micelles, Europhys. Lett. 12 (1990) 185.
[54] T. Imae, The flexibility of rodlike micelles in aqueous solutions and the crossover concentrations among dilute, semidilute, and concentrated regimes, Colloid Polym. Sci. 267 (1989) 707–713.

[55] C. Trozzi, G. Ciccotti, Stationary nonequilibrium states by molecular dynamics. II. Newton's law, Phys. Rev. A. 29 (1984) 916–925.
[56] B.D. Todd, D.J. Evans, P.J. Daivis, Pressure tensor for inhomogeneous fluids, Phys. Rev. E 52 (1995) 1627–1638.
[57] J. Zhang, J.S. Hansen, B.D. Todd, P.J. Daivis, Structural and dynamical properties for confined polymers undergoing planar Poiseuille flow, J. Chem. Phys. 126 (2007) 1–14, 144907.
[58] T. Yamamoto, K. Sawa, K. Mori, Velocity measurements for shear flows of CTAB/NaSal aqueous solutions between parallel plates, J. Rheology 53 (2009) 1347–1362.
[59] J. Delhommelle, J. Petravic, D.J. Evans, Reexamination of string phase and shear thickening in simple fluids, Phys. Rev. E 68 (2003) 031201:1–031201:6.
[60] J. Delhommelle, J. Petravic, D.J. Evans, Non-Newtonian behavior in simple fluids, J. Chem. Phys. 120 (2004) 6117–6123.
[61] J.-F. Berret, Molecular gels, in: R.G. Weiss, P. Terech (Eds.), Materials with Self-assembled Fibrillar Networks, Springer, 2006.
[62] D. Bonn, J. Meunier, O. Greffier, A. Al-Kahwaji, H. Kellay, Bistability in non-Newtonian flow: rheology of lyotropic liquid crystals, Phys. Rev. E 58 (1998) 2115–2118.
[63] S. Lerouge, J.-P. Decruppe, P. Olmsted, Birrefringence banding in a micellar solution or the complexity of heterogeneous flows, Langmuir 20 (2004) 11355–11365.
[64] D.M. Heyes, Transport coefficients of Lennard–Jones fluids: a molecular dynamics and effective hard sphere treatment, Phys. Rev. B 37 (1988) 5677–5696.
[65] L.V. Woodcock, Origins of thixotropy, Phys. Rev. Lett. 54 (1985) 1513–1516.
[66] D.J. Evans, G.P. Morriss, Shear thickening and turbulence in simple fluids, Phys. Rev. Lett. 56 (1986) 2172–2175.